Final Draft

of the original manuscript:

Goushegir, S.M.; dos Santos, J.F.; Amancio-Filho, S.T.:

Influence of process parameters on mechanical performance and bonding area of AA2024/carbon-fiber-reinforced poly(phenylene sulfide) friction spot single lap joints

Influence of process parameters on mechanical performance and bonding area of AA2024/carbon-fiber-reinforced poly(phenylene sulfide) friction spot single lap joints

S.M. Goushegir[a,b], J.F. dos Santos[a], S.T. Amancio-Filho[a,b,c] [*]

[a] Helmholtz-Zentrum Geesthacht GmbH, Institute of Materials Research, Materials Mechanics, Solid State Joining Processes, Geesthacht, Germany
[b] Helmholtz-Zentrum Geesthacht GmbH, Institute of Materials Research, Materials Mechanics, Solid State Joining Processes, Advanced Polymer-Metal Hybrid Structures Group, Geesthacht, Germany
[c] Hamburg University of Technology, Institute of Polymer Composites, Hamburg, Germany
[*] Corresponding author: Email: sergio.amancio@hzg.de Tel./Fax - +49 4152 87-2066 / - 2033

Abstract

Friction spot joining has been shown to be a potential technology to produce metal-composite hybrid joints. In this study, the effects of friction spot joining process parameters on the bonding area and mechanical performance of single lap joints were investigated using full-factorial design of experiments and analysis of variance. The main process parameters with significant influence on the bonding area were joining pressure, tool rotational speed and joining time. Joints with ultimate lap shear forces varying between 1698 ± 92 N and 2310 ± 155 N were obtained. Tool rotational speed and joining pressure displayed the highest influence on the lap shear strength of the joints followed by tool plunge depth, whereas the joining time was not statistically significant. The interaction between the rotational speed and joining time was the only interaction with a significant effect on the mechanical performance. Furthermore, the displacement at peak load and joint failure energy changed from 0.5 ± 0.0 mm to 0.8 ± 0.1 mm and 0.55 ± 0.04 to 0.97 ± 0.12 J, respectively, suggesting brittle fracture of the joints. In general, a larger bonding area as a result of higher heat input led to increased mechanical performance. The generated regression model by the analysis of variance was used to identify an optimized set of parameters for increasing the lap shear strength of the joints. Finally, it was demonstrated that higher heat input increased the amount of voids and defects in the joints because of the higher amount of entrapped air in the low viscosity molten polymer, as well as the large difference in the shrinkage properties of the matrix and carbon fibers. However, no correlation was observed between the area fraction of the voids and mechanical performance because the strength of the joints is dominated by the bonding area. Furthermore, the process temperature was monitored, which varied in the range of 370°C to 474°C.

1. Introduction

Lightweight structures are increasingly demanded in a wide range of engineering applications, such as the transportation industry [1-3], wind power towers [4] and bridge construction [5]. Especially in the transportation industry, where energy efficiency is required, the use of advanced polymers and their respective composites, such as carbon-fiber-reinforced plastics (CFRP), is rapidly growing due to their inherent capacity to reduce the weight of an engineering structure, such as an aircraft or car. In addition to the lightweight characteristic of the composites, they possess outstanding corrosion resistance, environmental stability, and high fatigue performance, making them attractive for various industries [6, 7]. On the other hand, lightweight metals such as aluminum, titanium and magnesium alloys are being further developed to reduce the weight of a structure while maintaining high mechanical performance. The development and employment of different materials with a diverse range of properties helps designers to select the right combination of materials to fulfill the required properties for the desired structure [6]. Despite the benefits of using different materials in a structure, joining of such dissimilar materials such as metal alloys and composites is a great challenge [2].

Traditional joining technologies such as bonding or mechanical fastening exhibit technological and environmental limitations. For instance, the curing time of an adhesive for structural adhesive bonding is a major shortcoming, among others. In addition, bonding of thermoplastic composites requires special pre-treatments to increase the intrinsic adhesion between the composite and the adhesive that improve the wettability and surface tension of the thermoplastics [8]. Problems in mechanical fastening of metal-composite joints have also been reported for the Airbus A380 [6]. During the developmental phase of the A380 wing, composite ribs were joined to the metal skin via aluminum brackets by bolting. During operation, some cracks appeared in the brackets, which could have led to failure of the entire component. Therefore, alternative and advanced joining technologies suitable for such hybrid structures are required to overcome or reduce the limitations of traditional techniques.

Friction spot joining (FSpJ) is an alternative joining technology to produce metal-composite joints, which was patented and developed at Helmholtz-Zentrum Geesthacht, Germany [9]. Some of the advantages of this new joining process include short joining cycles (in the range of 2 to 8 s), no need for filler materials, absence of emissions, low cost machinery and being environmental friendly [10]. In previous publications, it has been shown that the process can successfully join Mg AZ31 [10], AA2024 [11] and AA6181 [12] to glass and carbon fiber-reinforced composites. In these works, the main characteristics of the process, bonding mechanisms, joint microstructure and mechanical properties were investigated and addressed. In particular, a simple model was proposed [11] to explain the different bonding zones present in a FSp joint. The bonding zones were divided into an adhesion zone (AZ), transition zone (TZ) and plastically deformed zone (PDZ), and the PDZ had the highest contribution to the joint strength because of the presence of different bonding mechanisms, i.e., macro- and micro-mechanical interlocking, as well as adhesion forces.

Statistical analysis through design of experiment (DoE) techniques coupled with analysis of variance (ANOVA) is a very helpful tool to understand the effects of process parameters on the behavior of the joints. DoE techniques have been used to elucidate different aspects of a joining process by altering the respective process parameters. Esteves *et al.* [12] recently investigated the influence of the FSpJ process parameters on the microstructure and mechanical performance of AA6181 and carbon-fiber-reinforced poly(phenylene sulfide) (CF-PPS) double lap joints using the Taguchi method. The authors found that the rotational speed of the tool had the highest influence on the lap shear strength of the joint, followed by the joining time, plunge depth and joining force. They argued that the rotational speed and joining time are responsible parameters for the heat input in the process, whereas the plunge depth controls the macro-mechanical interlocking between the joining parts because it influences the formation of the metallic nub. Anawa and Olabi [13] also used the Taguchi method to investigate the influence of the welding speed, laser power and focal position on the generated residual stresses in the heat affected zone in laser welding of dissimilar stainless steel and low carbon steel plates. The authors identified that the welding speed was the most influential parameter on the reduction of residual stresses, whereas the laser power also had a strong effect on the response. However, their findings showed that the focusing position was statistically insignificant. Dashatan *et al.* [14] performed statistical analysis according to a full-factorial DoE, along with ANOVA and the signal-to-noise ratio, to understand the influence of the tool rotational speed, tool plunge rate and dwell time on the friction stir spot weld strength between PMMA and ABS polymeric sheets. They concluded that all of the parameters significantly influenced the lap shear strength of the joints and fracture modes. Altmeyer *et al.* [15] also used a full-factorial approach to analyze the effects of friction riveting process parameters on the joint formation and mechanical performance of titanium rivets and a short carbon-fiber-reinforced PEEK composite. By employing ANOVA, the authors identified that higher rotational speed, forging time and forging pressure increased the pull-out force of the friction riveted joints. In addition, a correlation between mechanical performance and joint formation was determined.

The single lap shear joint geometry is widely used in the literature by different researchers to study joint mechanical performance due to its geometrical simplicity. However, no previous study has investigated the effect of joining parameters on the mechanical performance and bonding area of single lap shear friction spot joints for the selected joining partners. Therefore, the major objective of this study is to investigate the influence of FSpJ process parameters on the bonding area and mechanical performance of AA2024-T3/carbon-fiber-reinforced poly(phenylene sulfide) single lap joints. Full-factorial DoE and ANOVA were used to statistically assess the effects of the process parameters on the formation of a plastically deformed zone and the lap shear strength of the joints. Statistical models based on regression equations were established for both responses. The developed models were validated by new sets of joining parameters, and a set of joining parameters was achieved to optimize the strength of the single lap shear joints. Finally, the formation of defects during the joining process and their influence on the mechanical performance were briefly discussed.

2. Friction Spot Joining (FSpJ) process

The principles of the FSpJ process have been thoroughly explained in our previous publications [10-12]. Briefly, the process employs a tool consisting of three parts: a stationary clamping ring to hold the joining parts together, a sleeve and a pin that can rotate and move independently (Figure 1(a)). Before starting the joining process, the metal is overlapped on top of the composite, and the parts are clamped together against a backing bar. In the first step, the tool approaches the surface of the metal while the sleeve and pin rotate in the same direction. The sleeve starts to plunge into the metal while the pin retracts, plasticizing a volume of the metal around it as a result of the generated frictional heat between the rotating sleeve and the metal. The plasticized metal flows into the cavity left behind by the upward movement of the pin. In the second step, the plasticized metal is pushed downward to the original position by the pin. Finally, the tool is retracted, and the joint consolidates under pressure and cooling. The process steps are schematically illustrated in Figure 1(b). The top view of a sound FSp joint between aluminum and a CFRP is shown in Figure 2.
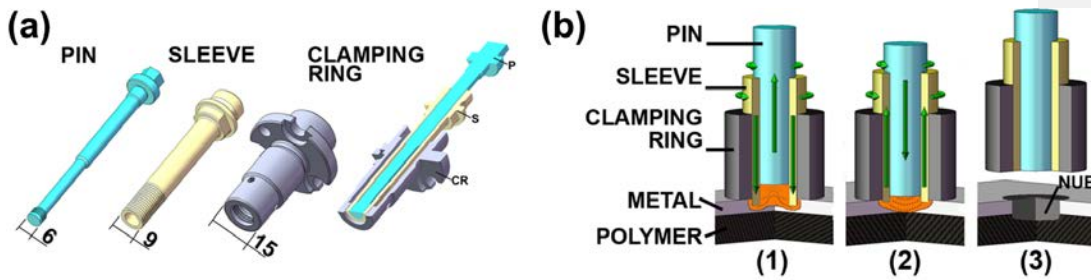

Figure 1. Schematic illustration of (a) FSpJ tool consisting of three parts; (b) FSpJ process steps: (1) the sleeve plunging softens the metal, (2) spot refilling and (3) joint consolidation [10].

Figure 2. Top view of a sound metal-composite friction spot joint.

The course of the process steps is graphically displayed in Figure 3, illustrating the variation of the tool (i.e., the sleeve and pin), rotational speed and position over time. As shown in the figure, in the first step, both the sleeve and pin approach the metal surface (position: 0 mm) while their rotational speed (solid line) increases to the predefined speed. In the second phase, the sleeve (dotted line) plunges into the metal (positive position) while the pin (dash-dotted line) retracts (negative position) upward. The third phase starts with the downward movement of the pin, which pushes the plasticized metal to the original position (position: 0 mm) while the sleeve retracts from the metal. Both the second and third phases together are considered the joining time in which the rotational speed of the tool is kept constant. Finally, in step four, the tool (both the sleeve and pin) is retracted upward from the surface of the metal, the rotational speed of the tool decreases, and the joint consolidates.
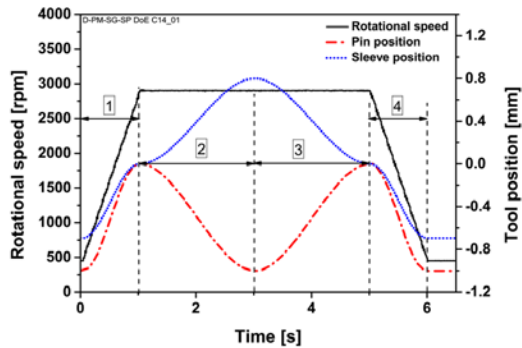
Figure 3. Example of a variation-monitoring diagram showing the FSpJ process phases.

Two phenomena occur during the process. First, the plasticized metal is deformed at the interface with the composite as a result of the axial movements and applied force of the tool, forming an undercut geometry in the shape of a metallic "nub". The nub is slightly inserted into the metal generating macro-mechanical interlocking between the joining parts [10, 11]. On the other hand, the generated frictional heat is conducted from the metal to the composite, causing the matrix of the composite to melt. The molten polymer is squeezed out over the bonding area, generating adhesion forces between the metal and composite after consolidation [10, 11].

The FSpJ process has four primary controllable parameters: the rotational speed (RS) of the tool, the sleeve plunge depth (PD) into the metal, the joining time (JT) and the joining pressure (JP). Controlling these parameters during joining is crucial in obtaining sound joints with the required mechanical performance due to their influence on the joint microstructure and bonding mechanisms. The general effect of each process parameter on the joint behavior can be found elsewhere [12].

3. Materials and methods

3.1. Base materials

The joining parts used in this work consist of two materials: an aluminum alloy and a thermoplastic composite. Rolled sheets of aluminum alloy (AA2024-T3) with a thickness of 2 mm (supplied by Constellium, France) were used as the metallic parts. This alloy is mainly used in the primary structures of aircrafts. AA2024 is a precipitation-hardenable alloy with Cu and Mg as the primary alloying elements. Heat treatment (T3) leads to the formation of strengthening phases such as Al_2CuMg and $CuAl_2$, which give rise to the high strength of this alloy [16]. The alloy exhibits a high strength to weight ratio, good fatigue resistance and damage tolerance, high fracture toughness, as well as good formability. However, the weldability of the 2xxx series of aluminum alloys including AA2024 by traditional fusion welding technologies is limited [17]. Advanced solid state welding techniques such as friction stir welding [18] and friction spot welding [19] are used to join the aluminum 2xxx series. Table 1 lists the nominal chemical

composition of the AA2024-T3 alloy used in this work, which was determined by chemical analysis. Some of the main mechanical and physical properties of the alloy are also given in Table 2. Figure 4(a) shows the microstructure of the alloy in longitudinal (L), transverse (T) and surface view (S) with respect to the rolling direction. It is possible to observe more elongated grains in the longitudinal direction compared with the equiaxed grains in the transverse direction and surface view.

Table 1. Nominal chemical composition of AA2024.

Element	Si	Fe	Cu	Mn	Mg	Cr	Zn	Ti	Al
wt%	0.1	0.17	4.55	0.45	1.49	<0.01	0.16	0.021	Bal.

Table 2. Selected mechanical and physical properties of the AA2024 used in this work.

Tensile strength (direction TL) [MPa]	Yield strength (direction TL) [MPa]	Elongation [%]	Melting onset [°C]	Thermal conductivity [$Wm^{-1}K^{-1}$]	Coefficient of thermal expansion within 20-300°C [K^{-1}]
437*	299*	21*	502**	121**	24.7**

* Experimentally evaluated.

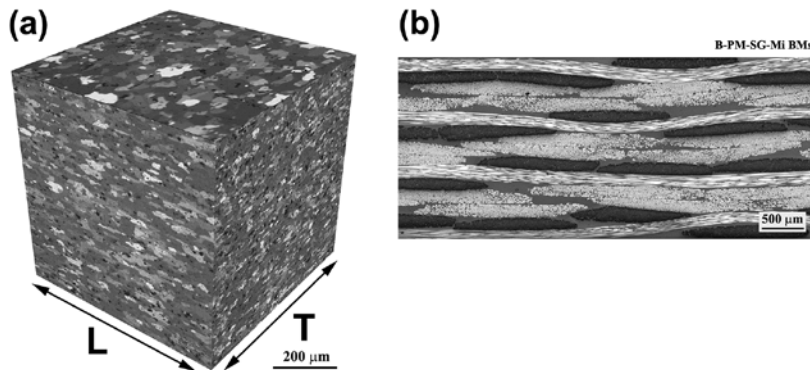** Data obtained from [17].

Figure 4. (a) Microstructure of AA2024 in longitudinal (L) and transverse (T) directions according to the alloy rolling direction, as well as the surface view; (b) microstructure of CF-PPS in the warp direction, showing fibers in 0°, 90° and ±45°.

In addition to the aluminum alloy, carbon-fiber-reinforced poly(phenylene sulfide) (CF-PPS) with 2.17 mm nominal thickness consisting of 5 harness woven quasi-isotropic laminates (supplied by Tencate, the Netherlands) with 50 vol% fibers was used as the composite partner. The composite consists of 7 plies of carbon fibers in the following sequence: [(0,90)/(±45)]$_3$/(0,90). CF-PPS is considered a high-performance semi-crystalline thermoplastic composite that is mainly used in primary and secondary aircraft parts because of its high strength, rigidity, chemical resistance and low water absorption [20, 21]. Table 3 lists some of the main mechanical and physical characteristics of the CF-PPS used in this work. The microstructure of the composite in the warp direction is shown in Figure 4(b).

Table 3. Selected mechanical and physical properties of the CF-PPS used in this work.

Tensile strength (warp) [MPa]	In plane shear strength [MPa]	Glass transition temperature [°C]	Melting temperature [°C]	Thermal conductivity [Wm^{-1}K^{-1}]	Coefficient of thermal expansion within 23-300°C [K^{-1}]
580*	119**	85*	285*	0.19**	52.2**

* Experimentally evaluated.

** Data obtained from supplier's datasheet [22].

3.2. Surface preparation

In our previous work [11], we showed that sandblasting can be used as an efficient pre-treatment on aluminum surfaces to increase the surface roughness and, hence, the micro-mechanical interlocking between the aluminum and the PPS matrix. Therefore, the aluminum surfaces were sandblasted prior to joining using corundum (Al$_2$O$_3$) particles with an average particle size in the range of 100 to 150 μm (provided by wiwox GmbH, Germany). The following parameters were used to blast the aluminum surfaces: blasting pressure of 6 bar, time of 10 s and distance between aluminum and the nozzle of approximately 25 cm. The angle between the aluminum specimens and the blasting nuzzle was set at 45°. After sandblasting, the specimens were blown with compressed air to remove the remaining sand particles, followed by acetone cleaning in an ultrasonic bath for 3 minutes and drying in air. The average surface roughness of the aluminum samples after sandblasting from five different samples was 5.2 ± 0.4 μm. The composite parts were also cleaned in an acetone ultrasonic bath for 3 minutes and dried in air.

3.3. Joining procedure

Friction spot joints were produced using a displacement-controlled machine (RPS100, Harms&Wende, Germany). First, the aluminum part was placed on top of the composite in the overlap configuration against a backing bar. The joining parts were clamped together during and after the joining cycle to ensure an intimate contact and to avoid separation of the parts during the cooling phase as a result of the different coefficients of thermal expansion of the selected

materials. A cooling phase of two minutes was selected after the joining cycle to ensure joint consolidation and to avoid any differential contraction.

3.4.   Temperature measurements

The process temperature was monitored on the surface of the aluminum using an infrared camera (VarioTHERM camera, Jenoptik, Germany) in the range of 150 to 700°C with a resolution of 256 × 256 pixels at 50 Hz. Figure 5 schematically illustrates the measurement set up and the position where the temperature was captured on the surface of the aluminum. The figure also shows a snapshot of a thermogram in which the measurement area is indicated. The peak temperature in the selected area was reported as the process temperature.
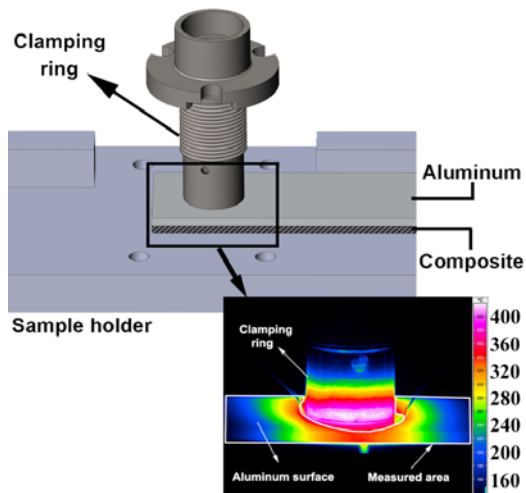
Figure 5. Schematic of the set up for infrared thermography and an example of a snapshot from the peak temperature on the aluminum surface during FSpJ. The area used to measure the temperature is indicated in the snapshot.

3.5.   Microstructural analysis

To analyze the microstructure, the joints were cut in the middle of the spot parallel to the aluminum rolling direction and prepared according to standard materiallographic procedures. Light optical microscopy (DM IR microscope, Leica, Germany) was used to analyze the cross-section of the joints under reflective light.

The voids, pores and defects were also analyzed and quantified from the cross-sections of the joints. To quantify the area fraction of the defects, each cross-section was transformed to a

binary image, and the contrast was set such that the defects were identified and distinguished from the carbon fibers. The cross-sectional area of the defects was quantified using ImageJ software. Figure 6 shows as an example the selected area from the cross-section of a joint containing defects and the respective generated binary image. The dark areas in the binary image correspond to the defects in the joint.
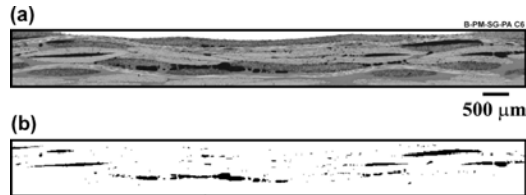

Figure 6. Illustration of (a) a cross-sectional micrograph of a joint in the area containing defects and (b) the generated binary image to quantify the defect area fraction.

3.6. Mechanical performance of the joints

The mechanical performance of the joints was evaluated based on overlap tensile shear testing according to the standard ASTM: D3163-01 using a universal testing machine (Zwick Roell model 1478) with a load capacity of 100 kN. The traverse test speed was 1.27 mm/min, and the tests were performed at room temperature. Three replicates were used to obtain the average ultimate lap shear force (ULSF) of the joints. Aluminum and composite specimens with the dimension of 100 × 25.4 mm^2 were machined for joining and subsequent single lap shear testing. The overlap area of the joints was 25.4 × 25.4 mm^2. For mechanical testing, a free distance of 150 mm between the grips was used. Figure 7 depicts an example of the load-displacement curve obtained from lap shear testing of the joints in which the ULSF is indicated as the peak force that a joint can bear before final failure. The displacement of the joints was also determined at the peak force from the load-displacement curve, which was obtained from the crosshead displacement of the tensile machine. Moreover, the failure energy of the joints was determined from the area below the load-displacement curve. Note that the maximum displacement was considered the displacement at the peak load and not the displacement at the failure.
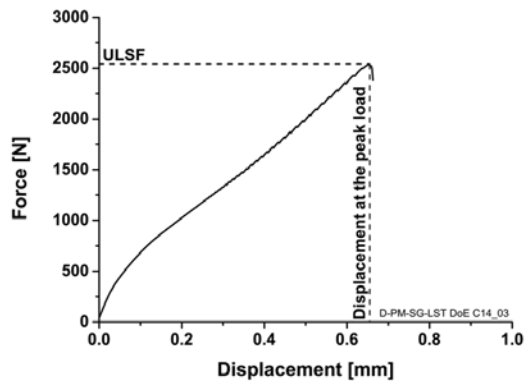
Figure 7. A typical load (force)-displacement curve acquired from lap shear testing of the joints with an indication of how the ULSF and displacement at the peak load were obtained. The joint failure energy was calculated from the area under the load-displacement curve.

3.7.   Fracture surface analysis

As explained before, a friction spot joint consists of three zones in the bonding area. Figure 8(a) schematically illustrates the bonding zones in an ideal condition, whereas Figure 8(b) displays an example of a real fracture surface of an FSp joint after mechanical testing. To simplify the visualization, the PDZ and TZ are indicated by solid ovals on the composite side, and AZ is marked by a dashed oval on the aluminum side. As previously mentioned, the plastically deformed zone (PDZ) is considered the strongest part of the joint. Therefore, the area of the PDZ was measured for all of the joints from the inner ring shown in Figure 8(b). To compare the PDZ area of the joints based on the tool used in this work, the area was normalized to the area of the sleeve ($63.6 \ mm^2$). The normalized PDZ area was used in the statistical analysis.
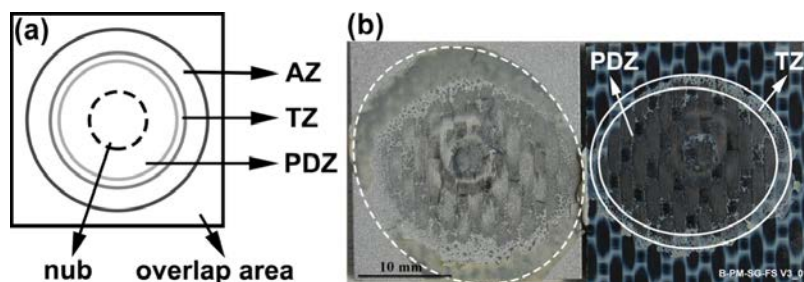

Figure 8. (a) Schematic illustration of an FSpJ fracture surface in which the bonding zones are indicated; (b) a real fracture surface: the transition zone (TZ) and plastically deformed zone (PDZ) are indicated by solid ovals on the composite side, whereas the dashed oval on the aluminum shows the AZ region.

3.8. Statistical analysis and process optimization for the bonding area and mechanical performance

Complex physical processes such as welding and joining consist of many parameters that influence the joint behavior. In most cases, the parameters interact with each other, which makes it difficult to analyze their effect on the joining process. Design of experiment (DoE) techniques and statistical analysis help to better understand the influence of process parameters and their interactions on the selected response while minimizing the number of required experiments. Among different design of experiments techniques, full-factorial design is considered as a powerful tool that can analyze both the effect of each process parameter and the influence of interaction between the parameters on the response [23]. This approach is especially helpful in the development phase of a new process to minimize the range of process parameters.

In this work, the experiments were proposed according to a full-factorial design with four parameters each at two levels and an additional center point, which led to 17 different conditions. The parameters (factors) used to evaluate their influence on the selected responses along with their corresponding levels are listed in Table 4. The selected responses analyzed were the normalized PDZ area and the ultimate lap shear force of the joints obtained from single lap shear testing. Table 5 shows all 17 experimental conditions given by the full-factorial design. In this work, three replicates for both the corner points and the center point were used to statistically analyze the results. ANOVA was used for statistical analysis of the results and to elaborate upon the influence of each process parameter and their interactions on the selected responses. A confidence interval of 95% was selected for the analysis, which means the influence of factors with a p-value less than 0.05 are considered statistically significant while those with a p-value above 0.05 are statistically insignificant [24] and were not included in the discussions. Table 6 lists the average and standard deviation results of the responses for all 17 joining conditions.

Table 4. FSpJ process parameters (factors) and their respective levels used in the 2^3-full factorial design of experiments in this work.

Factor (process parameter)	Symbol	Unit	Level 1	Level 2	Level 3
Rotational speed	RS	rpm	1900	2400	2900
Plunge depth	PD	mm	0.5	0.65	0.8
Joining time	JT	s	4	6	8
Joining	JP	MPa	0.2	0.25	0.3

pressure					

Table 5. Full-factorial DoE matrix listing the 17 given joining conditions.

Joining condition	Factors (process parameters)			
	RS (rpm)	PD (mm)	JT (s)	JP (MPa)
1	1900	0.5	4	0.2
2	2900	0.5	4	0.2
3	1900	0.5	8	0.2
4	2900	0.5	8	0.2
5	1900	0.5	4	0.3
6	2900	0.5	4	0.3
7	1900	0.5	8	0.3
8	2900	0.5	8	0.3
9	1900	0.8	4	0.2
10	2900	0.8	4	0.2
11	1900	0.8	8	0.2
12	2900	0.8	8	0.2
13	1900	0.8	4	0.3
14	2900	0.8	4	0.3
15	1900	0.8	8	0.3
16	2900	0.8	8	0.3
17	2400	0.65	6	0.25

4. Results and discussion

4.1. Temperature history

Monitoring the temperature during the FSpJ process is important to understand the influence of the process on the properties of the composite. Figure 9 illustrates the average peak temperature measured on the surface of the aluminum. The process temperature varied between 370°C and 474°C. The temperature in each condition was high enough to allow the deformation of aluminum under the tool and the formation of the metallic nub (process temperature varying between 0.7 incipient T_m and 0.9 incipient T_m of Al 2024). In addition, in all conditions, the process temperature was far above the melting temperature of PPS (T_m = 280°C), which allowed the melting of the PPS matrix close to the interface with aluminum, in a region around the nub. Nevertheless, even the highest temperature achieved (474°C) in condition 16 is below the onset of degradation temperature of CF-PPS. The average onset degradation temperature of 516°C was measured for the composite part by thermogravimetric analysis (results to be published in a separate manuscript), which is in agreement with the results reported in the literature for the PPS matrix (onset temperature above 500°C) [25, 26]. Furthermore, considering that the heating and cooling rates during the process are very fast (97°C/s and 17°C/s, respectively), extensive thermal degradation of the PPS matrix is not expected in the selected range of parameters in this study.
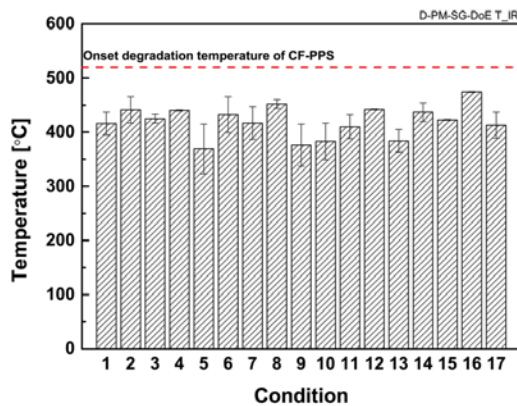

Figure 9. Average process peak temperature for the joining conditions.

4.2.   Influence of the process parameters on the selected responses

In this section, the influence of process parameters, i.e., rotational speed, plunge depth, joining time and joining pressure, on the normalized PDZ area and ULSF is discussed.

4.2.1.   Influence of the process parameters on the PDZ area

The results of the normalized PDZ area are listed in Table 6, which shows variation between 2.1 and 4.1. To statistically assess the results, an analysis of variance (ANOVA) with a confidence

level of 95% was carried out. The analysis suggested that RS, JT and JP have significant influence on the PDZ area because the p-value for all of these three factors was 0.000. However, the p-value for the PD was 0.429, suggesting that the influence is not significant. In addition to the main parameters, the only interaction between the factors with a significant effect on the response was PD×JT (p-value of 0.043). All of the other interactions resulted in a p-value above 0.05 and hence were not considered to significantly influence the PDZ area. Furthermore, the p-value of the curvature was 0.473, which means that, in the selected range, the effect of the parameters on the response can be explained linearly.

Table 6. Summary of the normalized PDZ area and ULSF for all of the 17 joining conditions.

Joining condition	Normalized PDZ area		ULSF (N)	
	Average	STD.	Average (N)	STD. (N)
1	2.1	0.3	1905	125
2	2.8	0.4	1977	108
3	3.2	0.4	1830	96
4	3.5	0.4	1825	27
5	2.9	0.5	1941	115
6	3.7	0.3	2172	193
7	3.7	0.3	1698	92
8	4.1	0.4	2310	155
9	2.5	0	1981	107
10	2.9	0.1	2140	138
11	2.7	0.1	1931	113
12	3.8	0.7	2002	22
13	3.5	0.5	2049	292
14	4.1	0.1	2280	88
15	3.3	0.0	2019	225
16	4.1	0.2	2143	168

| 17 | 2.8 | 0.4 | 2075 | 139 |

Figure 10 illustrates the main effect plots of the process parameters on the PDZ area. It is apparent from the figure that RS, JT and JP significantly influence the PDZ area; however, the effect of PD is insignificant. In these plots, a larger slope of the line indicates a stronger effect of the parameter on the response. On the other hand, when the slope of the line is close to zero, the effect is considered statistically insignificant.
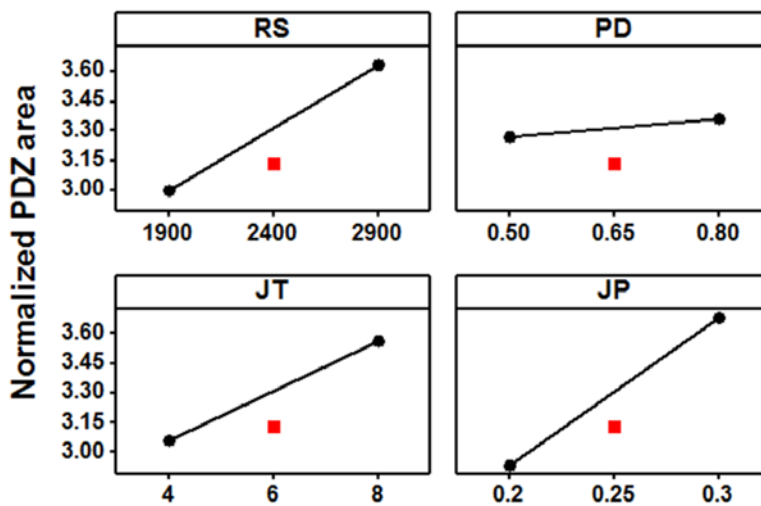

Figure 10. Main effect plots illustrating the influence of FSpJ process parameters on the normalized PDZ area.

Heat input during the joining process may be used to explain these results. Heat input is an important parameter in all solid-state joining processes because it governs the temperature in the joining area and therefore the local and global properties of the joining parts. Equation 1 shows the thermal model used for the friction stir spot welding (FSSW) process [27]. Because of the similarities in heat generation between FSpJ and FSSW, this equation can be used to explain the effect of the FSpJ process parameters on heat generation.

$$Q = \sum_{n=1}^{N} M(n)\omega(n)\Delta t \tag{1}$$

Q is the generated heat during the joining process, M is the torque (N.m), ω is the rotational speed (rad/s) of the tool, Δt refers to the joining time, and N is the total number of experiments. It can be observed from the equation that RS and JT directly control the heat input: increases in both of them increases the heat input in the process. It has also been discussed that the

increase in temperature as a result of heat generation by solid friction is proportional to the reverse of the thermal conductivity of the material [28, 29]. Due to the low thermal conductivity of the PPS, the conducted heat from the aluminum to the interface is not dissipated to the surrounding environment, which leads to a higher temperature in a volume of the composite at the center of the joint. Therefore, a reduction in the viscosity of the generated PPS molten layer is expected. This result is in agreement with the findings of Hou *et al.* [30]. The authors found that the apparent viscosity of the PPS is dependent both on the shear rate and temperature. The authors explained that PPS is a pseudoplastic polymer whose rheological behavior changes to be more Newtonian at elevated temperatures because of increase in chain motion. The low viscosity PPS molten layer flows easier and spreads out laterally outward in a larger area under the applied joining pressure. However, after a short time, the viscosity of the flowing PPS layer starts to increase (because of the very fast cooling rate after the joining process), which leads to the formation of the TZ before the final consolidation of the layer in the AZ region. Figure 11 depicts the relationship between the normalized PDZ area and the process temperature. In general, trend the PDZ area increases with increasing the process temperature, as discussed above.
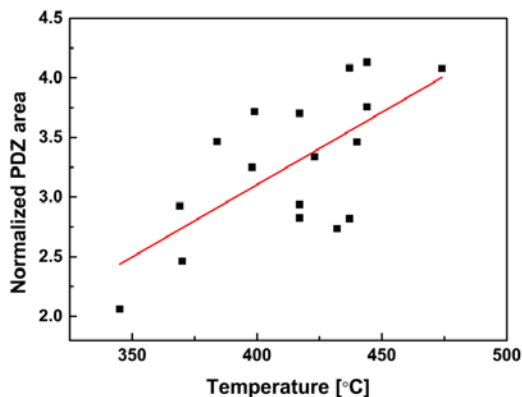

Figure 11. Normalized PDZ area-process temperature relationship. Generally, higher temperatures lead to a larger PDZ area.

From the statistical analysis, the joining pressure showed the highest impact on the area of the PDZ because the slope of the JP in Figure 10 is steeper than the other parameters. The flow of the PPS matrix molten layer while the viscosity is still low is the key factor to enlarge the PDZ area. As soon as the PPS viscosity increases, the air entrapped in the highly viscous molten layer cannot escape, which leads to a larger TZ and a reduced PDZ area. In addition to the rotational speed of the tool, which causes the reduction in the viscosity of the PPS molten layer, the axial force in the spot area (as a result of the JP) facilitates the outward flow of the PPS layer. Similar behavior was reported for spin welding [28] and vibration welding [31] of thermoplastics for which higher welding pressure causes faster lateral flow of the molten polymer. It seems that in FSpJ, both factors, i.e., high rotation of the tool and large JP, are required to increase the spreading of the molten polymer. When the JP is low, the lateral flow is

slow while the viscosity increases rapidly due to the heat losses. Therefore, a large TZ with a large amount of entrapped air pockets is the result of low JP, as shown in Figure 12(a) in which the lowest JP level (0.2 MPa) was used (condition 4). In contrast, higher JP and the resulting tool axial force facilitates the flow of the molten layer with low viscosity and hence a larger PDZ. Figure 12(b) shows the fracture surface of condition 8, which has the same parameters as condition 4 but with higher JP (0.3 MPa). It is obvious from the figure that higher JP leads to a larger PDZ and smaller TZ by facilitating the flow of the low viscosity PPS molten layer. The normalized PDZ area in Figure 12 shows an 18% increase (from 3.5 to 4.1) by increasing the JP from (a) 0.2 MPa to (b) 0.3 MPa.
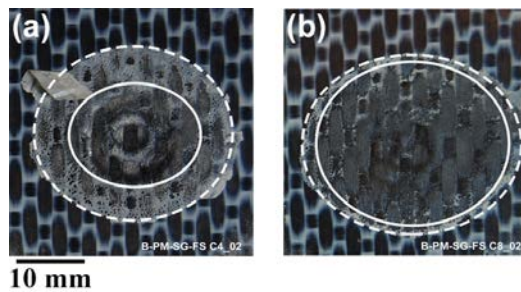

Figure 12. Indication of the PDZ (solid oval) and TZ (dashed oval) area on the fracture surface (composite side) of (a) condition 4, JP: 0.2 MPa and (b) condition 8, JP: 0.3 MPa.

From the ANOVA analysis, the only interaction with a significant influence on the PDZ area was PD×JT, as observed in the interaction plot in Figure 13. This result may be explained by the fact that increasing the PD increases the exerted axial force on the aluminum beneath the tool and hence on the molten polymer in the spot area, which will flow at higher rates.

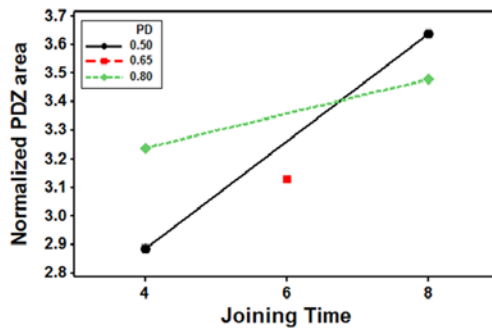
Figure 13. Interaction plot illustrating the influence of PD × JT on the normalized PDZ area.

When the joining time is short (4 s) the molten PPS does not have enough time to maintain a low enough viscosity, and the out-flow rate reduces faster. In this case, a higher PD may

facilitate the flow rate by increasing the applied axial force in addition to the exerted force by JP. Figure 14 shows an example of the fracture surface of two joints with similar joining parameters produced with shorter JT (RS: 2900 rpm, JP: 0.3 MPa, JT: 4 s). However, the PD in (a) is 0.5 mm, whereas the PD in (b) is 0.8 mm. It was observed that increasing the PD at short JT increases the normalized PDZ area by approximately 11% (from 3.7 to 4.1).
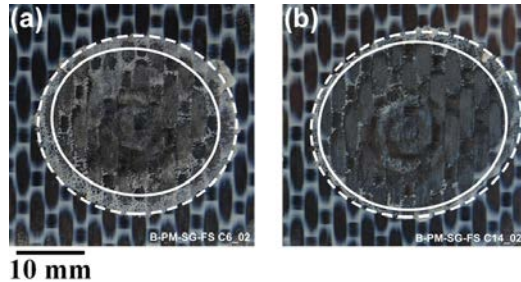

Figure 14. Fracture surface (composite side) of (a) condition 6, PD: 0.5 mm and (b) condition 14, PD: 0.8 mm. Solid ovals indicate the PDZ area, and the dashed ovals refer to the TZ.

The influence of the PD was reversed when the JT increased to 8 s. At a JT of 8 s, the average PDZ area slightly increases (approximately 3%) by changing the PD from 0.8 mm to 0.5 mm; however, the means of normalized PDZ area lie in the range of the standard deviation (3.5 ± 0.5 for PD of 0.8 mm and 3.6 ± 0.3 for PD of 0.5 mm). This result is because prolonged JT (at 8 s) may keep the viscosity of the molten PPS low for a longer period; therefore, the applied force from the JP is sufficient to spread the molten PPS layer in the overlap area.

4.2.2. Influence of the process parameters on the Ultimate Lap Shear Force (ULSF)

The results of the ULSF are also listed in Table 6 with a variation between 1698 ± 92 N and 2310 ± 155 N. The performed ANOVA showed that RS, JP and PD have the most significant influence on the ULSF with the p-values of 0.000, 0.013 and 0.031, respectively. However, the p-value of 0.080 for the JT suggested that its influence is insignificant on the ULSF in the selected range of experiments. Furthermore, the interaction of RS×JP with the p-value of 0.026 is the only interaction with significant influence. In addition, the curvature showed a p-value of 0.675, which suggests that the relationship between the response and the factors is linear.

Figure 15 illustrates the main effects of the process parameters on the ULSF response. Increasing in RS, PD and JP increases the ULSF, whereas increasing the JT reduces the ULSF. The comparison between the influence of process parameters on the responses shows that RS and JP significantly influence both the PDZ area and the ULSF (compare Figures 10 and 15). Increases in RS and JP lead to an increase in the PDZ area and ULSF, whereas the effect of JT is reversed. In addition, although PD did not show a significant influence on the PDZ area, it has a major effect on the mechanical performance of the joints. The influence of the

statistically significant parameters on the ULSF and the differences in their effect on the PDZ area will be discussed in the following section.
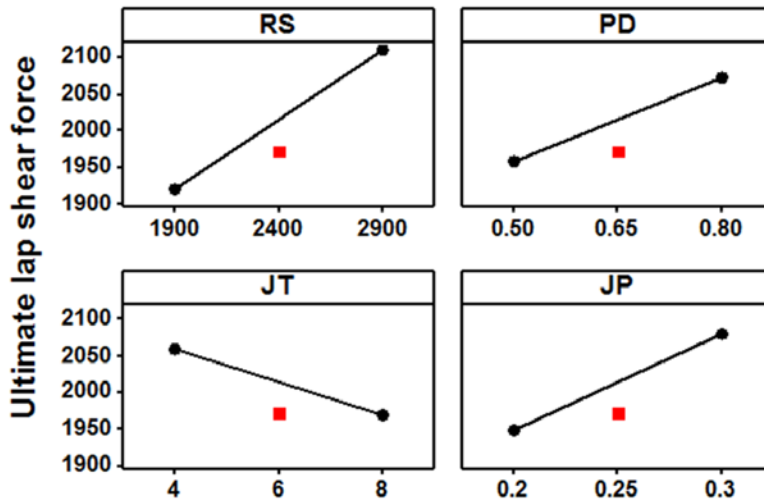

Figure 15. Main effect plots illustrating the influence of FSpJ process parameters on the ultimate lap shear force.

As discussed in the previous section, increasing the RS increases the PDZ area because of the higher heat input (see Equation 1) and resultant lower molten PPS viscosity. As previously reported [11], the PDZ area is the strongest part of the joint. In the FSpJ, it is desirable to extend this zone. Figure 16 depicts the relationship between the PDZ area and ULSF for the 17 DoE joining conditions. There is a clear trend that a larger PDZ area increases the ULSF of the joints. This result may be explained by the fact that larger PDZ increases the contact area between the aluminum and the consolidated molten PPS, which causes higher adhesion forces and increased micro-mechanical interlocking of the PPS layer into the surface crevices of the pre-treated aluminum. These results are in accordance with our previous work [11] that showed that increasing the RS of the tool continuously increases the bonding area and hence the lap shear strength of the joints. Nevertheless, the results of this work are in contrast with the findings of Esteves *et al.* [12] on the FSpJ of the same composite with the aluminum alloy 6181-T4. In their work, the lap shear strength of the joints increased by increasing the RS of the tool up to a certain speed followed by a reduction in strength by further elevating the RS. The authors argued that this behavior is a result of the well-known slip phenomenon reported for friction stir spot welding of aluminum alloys [32, 33]. In such cases, slipping occurs between the rotating tool and aluminum when the RS increases due to the reduction of the viscosity or local melting of the aluminum in contact with the tool. Slip phenomenon leads to a reduced heat input and hence decreased mechanical performance. However, in our work, this behavior was not observed possibly because of the higher strength of the AA2024-T3 and the level of heat inputs

achieved as a result of the range of the selected joining parameters. These factors may have prevented the achievement of the slipping transition in the current study.
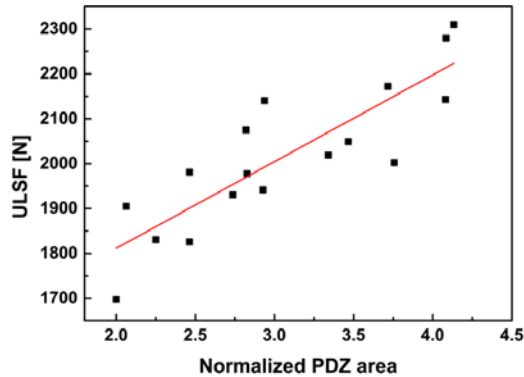

Figure 16. Relationship between the ULSF and the normalized PDZ area. Increasing the PDZ area increases the ULSF.

The joining pressure is another parameter with a high influence on the lap shear strength of the joints. As explained in the previous section, the exerted axial force by applying sufficient JP facilitates the squeezing flow of the molten PPS, which therefore leads to a larger PDZ. In addition to the larger PDZ, another explanation of the influence of the JP on the ULSF is given in [12]. This result has been explained by the fact that higher JP facilitates the flow of the molten PPS into the pores and crevices on the surface of the aluminum. Improved wetting and pore filling increases the micro-mechanical interlocking as one of the main bonding mechanisms. However, in contrast with the work of Esteves *et al.* [12] that states that the strength of the joints showed less sensitivity to the JP, the findings of the current study show that JP has a significant influence on the ULSF of the AA2024-T3/CF-PPS friction spot joints. In addition to the differences between the aluminum alloys used in both studies, the range of the JP is also different (higher in this study). Esteves *et al.* [12] used a JP in the range of 0.2 MPa to 0.24 MPa, whereas it was varied between 0.2 MPa and 0.3 MPa in the current work. In addition, distinct surface pre-treatments were applied to the aluminum alloys: they were sandblasted and mechanically grinded by Esteves and co-workers [12]. In the current investigation, higher axial forces were required such that the molten PPS could completely penetrate into and wet fully larger pores and crevices on the sandblasted aluminum surface.

The plunge depth of the tool into the aluminum is also statistically significant when analyzing ULSF as the response. The PD influences the shape of the metallic nub and therefore the macro-mechanical interlocking between the aluminum and the composite. The formation of the metallic nub and its insertion into the composite entraps a part of the composite, which leads to the increased macro-mechanical interlocking and strength of the joints, especially under shear loading. Increasing the entrapped volume of composite increases the macro-mechanical interlocking. Consequently, higher lap shear strength of the joints will be obtained. Figure 17 shows the cross-section of two joining conditions (conditions 2 and 10 from the DoE

experiments, Table 5) whose plunge depths are (a) 0.5 mm and (b) 0.8 mm, respectively, while the other process parameters are equal. It is evident from the images that the shape and size of the nub (indicated by black ellipses) are different. Figure 17(c) illustrates a simplified schematic cross-sectional view of the nub with the entrapped composite (gray layer). Assuming the real 3D shape of the nub, the volume of the entrapped composite may be considered a circular truncated cone, which can be calculated from Equation 2.

$$V = \frac{1}{3} \pi \ (R^2 + r^2 + Rr) \tag{2}$$

where V is the volume of the entrapped composite, h is the height of the metallic nub, and r and R are the upper and lower radii, respectively.

Based on Equation 2, the entrapped volume for both conditions was calculated, which resulted in 3 mm^3 for condition 2 (PD: 0.5 mm) and 4.6 mm^3 for condition 10 (PD: 0.8 mm). Therefore, with the same process parameters, resulting in similar heat inputs, an increase of approximately 53% in the volume of the entrapped composite is achieved by increasing the PD from 0.5 mm to 0.8 mm. The higher amount of entrapped CF-PPS in the nub increased the macro-mechanical interlocking and hence the lap shear strength of the joints slightly from 1977 to 2140 N.
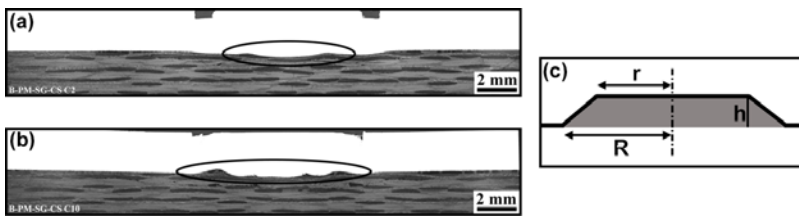

Figure 17. Cross-sectional micrograph of (a) condition 2, PD: 0.5 mm and (b) condition 10, PD: 0.8 mm. Ovals indicate the formed nub. (c) A simplified schematic illustration of the nub with the entrapped molten polymer (gray layer).

From the ANOVA analysis, the only interaction with a significant influence on the ULSF was RS×JP, as shown in Figure 18.
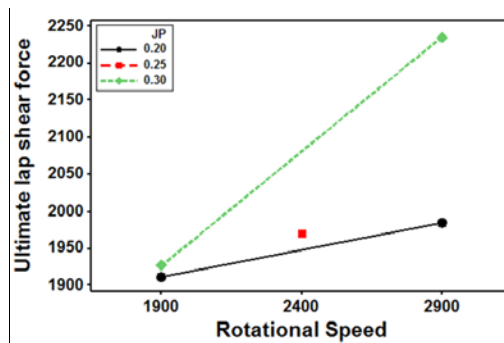
Figure 18. Interaction plot illustrating the influence of JP × RS on the ultimate lap shear force.

Although the exact reason for this result is still not well understood, current knowledge allows us to attribute the result to the viscosity and flow of the molten PPS.

From Figure 18, one can see that, at low RS (1900 rpm), increasing the JP does not show a significant change in the ULSF. However, there is a significant influence of the JP on the ULSF at higher RS (2900 rpm), as shown Figure 18. When the RS is high, the viscosity of the molten PPS is drastically reduced, and the lateral flow of the molten PPS is fast. In such a situation, a higher axial force is required to achieve and ensure intimate contact between the aluminum and the molten PPS layer to keep the low viscous polymer inside the pores of the aluminum. Because the generated crevices on the surface of the aluminum were in the range of several microns, a firm contact through applied JP leads to the optimal wetting of such crevices by the molten PPS. Figures 19 (a) and (b) show the cross-sections of the joints inside the PDZ area of conditions 2 and 6 with RS of 2900 rpm and JP of 0.2 MPa and 0.3 MPa, respectively. In the cross-section of condition 2 (Figure 19 (a)), a gap between the aluminum and the PPS is visible, which is indicated by the white dotted line between the gap and the PPS. In this case, the viscosity of the molten PPS is very low due to higher heat input, and there is no intimate contact between the aluminum and the composite because of the low JP. Therefore, the molten PPS rapidly flows in the lateral direction. Therefore, the applied pressure is not enough to result in optimal filling and wetting of the molten PPS in the crevices and pores of the aluminum. The presence of such a gap reduces the micro-mechanical interlocking and, consequently, the lap shear strength of the joints. In contrast, the pore filling and micro-mechanical interlocking is more efficient in condition 6 in which the JP is higher and the molten PPS is firmly pushed upward to the pores on the surface of the aluminum.

It is important to note that changes in the dynamic rheological and viscoelastic behavior of the composite as a result of altering the FSpJ process parameters are very complex and should be further investigated to better understand the flow of molten PPS during the process.
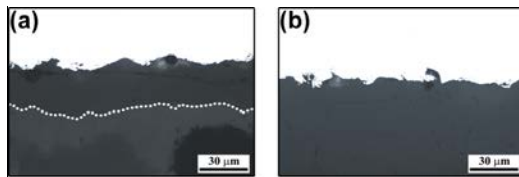

Figure 19. Microstructure of the joints at the interface between the aluminum and the composite: (a) condition 2, (b) condition 6 inside the PDZ. In (a), a gap between aluminum (white part) and the molten PPS is clear as a result of high heat input and low JP. The dotted line in (a) indicates the boundary between the gap and the molten PPS.

In addition to the improved wetting and increased micro-mechanical interlocking discussed above, the JP at higher RS influences the macro-mechanical interlocking. At a high RS of 2900 rpm, the local formability of the aluminum is increased as a result of higher heat input. In such situations, a change in JP alters the shape of the nub. Figure 20 shows, as an example, the

cross-section of two joints (conditions 4 and 8 from the DoE experiments, Table 5) with a RS of 2900 rpm and JP values of 0.2 MPa and 0.3 MPa, respectively. In the same manner, as explained in Figure 17 (c), the volume of entrapped PPS inside the nub was measured, which resulted in a volume of 0.35 mm^3 for condition 4 and 1.1 mm^3 for condition 8. This increase in the entrapped PPS inside the nub increases the macro-mechanical interlocking and hence the ULSF of the joint (from 1825 N for condition 4 to 2310 N for condition 8).

Furthermore, as discussed in the previous section, higher JP increases the PDZ area, which also contributes to the strength of the joints. Therefore, at higher RS, an increase in the JP promotes the bonding mechanisms in the joint, which leads to improved mechanical performance.
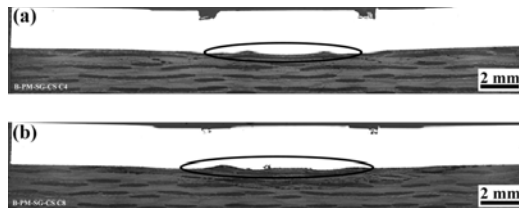

Figure 20. Cross-sectional micrographs of (a) condition 4, JP: 0.2 MPa and (b) condition 8, JP: 0.3 MPa. Ovals indicate the formed nub.

In summary, these results suggest that the highest level of the RS (2900 rpm), PD (0.8 mm) and JP (0.3 MPa) along with the lowest level of JT (4 s) may provide the optimized set of parameters to increase the lap shear strength of the FSp joints. This set of parameters corresponds to condition 14 of the selected DoE with the ultimate lap shear force of 2280 ± 88 N and the normalized PDZ area of 4.1 ± 0.1. On the other hand, the optimized set of parameters for the higher PDZ area is condition 16 with all parameters at their highest level. This condition provides a normalized PDZ area of 4.1 ± 0.2.

4.3. Model validation

The analysis of variance provided two models for the normalized PDZ area and ULSF in which these responses were the dependent variables and the joining parameters (RS, PD, JT, JP), and their interactions were the independent variables.

Figure 21 shows the Pareto charts for the normalized PDZ area and ULSF. The vertical lines in the charts correspond to the 95% confidence interval used to analyze the data sets. All of the parameters and their interactions with bars passing the vertical line are considered statistically significant for the selected response and are included in the ANOVA regression model. Note that for the ULSF model, although the joining time is considered an insignificant parameter, it is also included in the model because the JT is one of the main process parameters. Its inclusion slightly increased the accuracy of the model. Equations 3 and 4 express the regression models for the normalized PDZ area and ULSF, respectively.
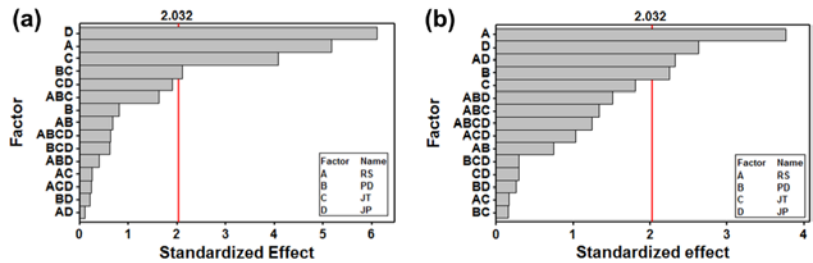
Figure 21. Pareto charts of the standardized effects for (a) normalized PDZ area and (b) ULSF.

normalized PDZ area $= -2.69108 + 0.000630833 \times RS + 2.89167 \times PD + 0.402431 \times JT + 0.744167 \times JP - 0.427778 \times PD \times JT$ (3)

$ULSF = 2847.53 - 0.464686 \times RS + 182.551 \times PD - 18.3718 \times JT - 627.598 \times JP + 0.298916 \times RS \times JP$ (4)

To validate the regression models from ANOVA, four new joining conditions were designed. The level of each joining parameter was randomly generated within the range of the DoE. Table 7 lists the validation joining conditions. The experimental results of the normalized PDZ area and the ULSF for these joining conditions are listed in Table 8.

Table 7. Four sets of joining parameters to validate the regression models.

Joining condition	Process parameters			
	RS (rpm)	PD (mm)	JT (s)	JP (MPa)
V1	2070	0.6	6.6	0.26
V2	2570	0.55	5.2	0.28
V3	2240	0.7	4.6	0.24
V4	2740	0.75	7.2	0.22

Table 8. Summary of the normalized PDZ area and the ULSF for the validation joining conditions.

Joining condition	Normalized PDZ area		ULSF (N)	
	Average	STD.	Average (N)	STD. (N)
V1	3.4	0.1	2001	137

V2	3.8	0.1	2007	118
V3	2.9	0.1	2257	336
V4	3.5	0.3	1975	343

Figure 22 presents the comparison between the experimental data for both responses and their respective predicted values obtained from Equations 3 and 4 for all of the 17 DoE conditions (x marks) and the four validation conditions (black circles). The middle 45° solid line shows the best linear relationship between the experimental and predicted values, whereas the dashed lines provide ±10% deviation from the perfect line. Altmeyer *et al.* [15] reported that a deviation of ±10% may be used to cover the mechanical properties variations in the plastics (in this case, the CF-PPS base material) produced within the same batch. There is a very good correlation between the experimental data and the predicted values for the PDZ area, as observed from Figure 22(a) in which most of the data points lie within ±10% from the best fit. The model could also predict the normalized PDZ area for all four validation conditions within the range of ±10% error. However, in case of the ULSF, there is more deviation present between the experimental and the predicted results, as shown in Figure 22(b) in which some of the data are not accurately predicted by the model. Nevertheless, three out of four validation experiments are predicted within ±10% error for ULSF.

In addition to the qualitative validation of the data in Figure 22, the goodness-of-fit in terms of the R-squared value of the regression models was also statistically analyzed considering a 95% confidence interval. The results showed that, for the PDZ area, the R-squared value of the model was 73%, whereas the R-squared value of the ULSF model was 70%. These values suggest that the accuracy of the models to predict the responses in the selected range of the joining parameters is approximately 70%, which is statistically acceptable. The quadratic effects of process parameters might be significant; therefore, their inclusion in the regression model might increase the R-squared value.
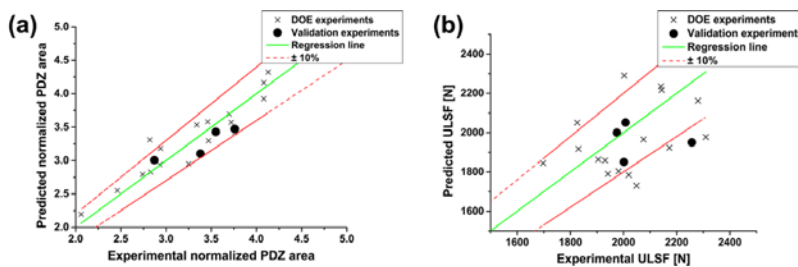

Figure 22. Predicted data from regression models vs. experimental results for (a) the normalized PDZ area and (b) the ULSF. Cross marks (x) illustrate the DoE joining conditions, whereas black dots refer to the results of the validation joining conditions.

5. Displacement, failure energy and defects formation in the joints

In addition to the bonding area and mechanical performance of the joints in terms of ultimate lap shear force, the relative displacement of the joints during mechanical testing, the absorbed energy until failure, and the generated defects are important issues. In this section, these aspects are briefly discussed; however, the intention is not to analyze the influence of the process parameters on these aspects.

The displacement at the peak load of the single lap shear joints varies from 0.5 ± 0.0 mm to 0.8 ± 0.1 mm, as observed from Table 9. The lowest displacement corresponds to condition 7 that has a RS of 1900 rpm during the joining process and lower heat input. In contrast, the conditions with higher RS (2900 rpm) and heat input show the highest displacement (conditions 2, 8, 14 and 16). In general, the conditions with higher heat input illustrate larger displacement because of the larger bonding area between the joining parts. In addition, the results of the failure energy show a similar trend to the displacement, varying between 0.55 ± 0.04 and 0.97 ± 0.12 J. Both of these results indicate brittle fracture for the friction spot joints by relatively low displacement at the peak load and a low to moderate amount of absorbed energy before failure. However, it is important to note that the CF-PPS joining partner itself is a brittle material [34, 35], having linear elastic behavior under tensile testing. Both the displacement at the peak load and the failure energy of the optimized condition (condition 14) proposed by the statistical analysis presented in section 4 show the high values of 0.8 ± 0.1 mm and 0.97 ± 0.12 J.

Table 9. Summary of the displacement, failure energy and pore area fraction results, as well as the ULSF to pore area fraction, for all of the 17 DoE joining conditions.

Joining condition	Displacement (mm)		Failure energy (J)		Pore area fraction		ULSF / pore area fraction
	Average (mm)	STD. (mm)	Average (J)	STD. (J)	Average (mm^2)	STD. (mm^2)	
1	0.7	0.1	0.81	0.06	0.09	0.00	0.022
2	0.8	0.1	0.87	0.06	0.49	0.03	0.004
3	0.7	0.0	0.76	0.06	0.18	0.01	0.011
4	0.6	0.0	0.60	0.02	0.18	0.01	0.010
5	0.6	0.1	0.65	0.09	0.26	0.02	0.007
6	0.7	0.1	0.69	0.09	0.57	0.03	0.003
7	0.5	0.0	0.55	0.04	1.00	0.03	0.002

8	0.8	0.1	0.80	0.18	1.00	0.09	0.002
9	0.6	0.0	0.75	0.07	0.03	0.00	0.071
10	0.6	0.0	0.69	0.07	0.55	0.03	0.004
11	0.6	0.0	0.62	0.04	0.45	0.04	0.004
12	0.6	0.0	0.75	0.01	0.77	0.07	0.003
13	0.7	0.11	0.61	0.09	0.52	0.04	0.003
14	0.8	0.1	0.97	0.12	0.91	0.04	0.002
15	0.7	0.2	0.67	0.05	0.71	0.06	0.003
16	0.8	0.1	0.95	0.14	1.00	0.02	0.002
17	0.7	0.0	0.84	0.07	0.63	0.04	0.003

The other issue that should be considered in joining polymer-metal hybrid structures is the presence of defects and voids in the joint, which has been reported by several researchers [36-40]. The area fraction of the voids in all of the conditions from the DoE was determined and presented in Table 9, showing a variation between 0.03 ± 0.00 mm^2 and 1.00 ± 0.09 mm^2. The results show that the conditions with higher heat input lead to a larger area fraction of the pores. Figure 23 shows the cross-section of two joints from conditions (a) 8 and (b) 9 with high and low heat input, respectively. It can be observed from the figure that higher heat input generates more voids and defects in the polymeric matrix of the composite volume adjacent to the aluminum (see Table 9). Furthermore, in case of condition 8, the heat affected zone through the thickness of the composite is approximately 1050 μm, which is 75% higher than that observed for condition 9 (600 μm). Considering that thermal degradation of the polymeric matrix is absent or reduced, this result might be explained by the fact that higher heat input reduces the viscosity of the PPS matrix; thereby, a higher volume of air is entrapped that turns to air pockets and voids after consolidation of the joint. The formation of voids as a result of air entrapment was also reported by Yusof *et al.* [36] in laser joining of polyethylene terephthalate and AA5052. In addition, mass transfer because of the squeezing flow of the molten polymer from the central region of the joint outwards may lead to the generation of some defects, as discussed by Ageorges *et al.* [37] in resistance welding of thermoplastics. In addition to the air entrapment and squeeze flow of the molten polymer, the presence of the volumetric defects has been reported to be a result of thermal degradation of the polymer matrix and evolution of structural water [41], although these aspects were not observed in this work. Another type of defect that has been identified is fiber-matrix debonding. It is believed that the large difference between the coefficients of thermal expansion between the fibers and the matrix may lead to this type of defect when the joining cycle is complete. Ye *et al.* [42] reported that a critical applied pressure is required during post-thermal processing of CF-PPS to avoid de-compaction of the fibers. This

critical pressure was theoretically estimated and reported to be 0.49 MPa for 5H satin CF-PPS laminates. This pressure is much higher than the range of joining pressure used in this work, which may be another reason for the fiber-matrix debonding observed in some FSp joints.
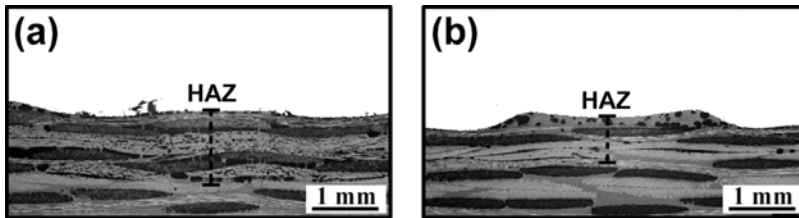

Figure 23. Cross-sectional micrograph of (a) condition 8 and (b) condition 9 with high and low heat input, respectively, showing the defects in the composite part.

An important subject is the influence of the defects on the mechanical performance of the joints. Generally, it is considered that the presence of voids and defects reduce the mechanical performance of the joints, as reported in [43]. However, no correlation between the area fraction of the pores and the lap shear strength of the joints could be established in this work. Figure 24 shows the cross-section of a fractured friction spot joint after lap shear testing (composite side). From the figure, one can see that the pores did not appear to act as stress concentrators and crack nucleation sites because the crack propagated at the interface of the metal-composite, within the volume of consolidated PPS matrix. In addition, the propagated crack did not interact with the voids and it altered its path around the large pore in Figure 24. It can be concluded that in FSpJ, increased heat input is increases the area fraction of pores; however, increased PDZ or bonding area is also obtained. We likewise illustrated that increased bonding area leads to increased lap shear strength of the joints (see Figure 16). This result is in accordance with the results demonstrated by Karachalios *et al.* [44] in adhesively bonded joints who showed that, in some situations, the size and shape of the defects did not significantly influence the global quasi-static strength of the joint, especially when the failure is dominated by the bonded area, by using a brittle adhesive.
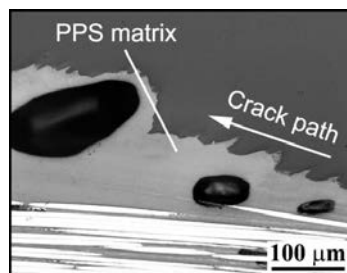

Figure 24. Magnified cross-section of a failed specimen (composite side) illustrating that the pores neither act as crack nucleation sites nor interact with the propagating radial crack.

Finally, the ultimate lap shear force of the joints was divided by the respective area fraction of the pores, and the results are reported in the last column of Table 9. Condition 9 showed the highest value because it possesses a low amount of defects (as a result of lower heat input) and relatively high lap shear strength.

6. Conclusions

The main goal of the current investigation was to statistically assess the influence of FSpJ process parameters on the formation of the PDZ area and the strength of AA2024-T3 / CF-PPS single lap shear joints. Full-factorial DoE and analysis of variance were employed for statistical analysis.

Friction spot joints with ultimate lap shear forces ranging from 1698 ± 92 N to 2310 ± 155 N were obtained. This study showed that the RS of the tool and the JT significantly influence the PDZ area because they control the heat input in the joints and therefore the viscosity of the molten PPS matrix. Higher RS and longer JT decrease the viscosity and facilitate the flow of the molten PPS to spread in the bonding area. JP is another important process parameter that was found to have a significant effect on the PDZ area. Higher JP in the investigated range increased the lateral flow of the molten PPS by exerting axial forces by the tool on the molten layer. It was also identified that the PD is insignificant in the selected range of process parameters. Furthermore, the interaction of the PD and JT was significant when analyzing the PDZ area. Low viscosity molten PPS as a result of short JT requires higher PD to increase the axial force and hence facilitates lateral flow of the molten PPS. On the other hand, at longer joining times, the effect of PD is less pronounced. In this case, prolonged JT maintains the low viscosity of the molten PPS for a longer time, and the exerted force from the applied JP is sufficient to spread out the molten PPS.

The study also found that the RS is the most important parameter affecting the ULSF of the joints because higher RS increases the heat input in the joints and therefore produces a larger PDZ area. A trend was observed where increasing the PDZ area increases the ULSF because the contact area, and therefore adhesion forces, between the aluminum and the composite is larger. The JP was shown to be the second most important parameter influencing the ULSF. Higher JP pushes the molten PPS into the pores and crevices on the surface of pre-treated aluminum and increases the micro-mechanical interlocking between the joining parts. It was found that PD also significantly contributes to the ULSF of the joints because it controls the shape and extent of the nub and therefore the amount of molten PPS entrapped inside the nub. Larger PD increases the mechanical interlocking through the entrapment of a larger amount of PPS in the nub; therefore, a higher ULSF is obtained. The investigation of the JT showed that its influence is insignificant on the ULSF in the selected range of parameters. Finally, the interaction between RS and JP significantly influenced the ULSF. This result was explained due to higher RS that reduces the viscosity of the molten PPS and requires higher JP to keep the molten PPS in intimate contact with the aluminum; therefore, increased pore filling and wetting, as well as optimal micro-mechanical interlocking were achieved. Based on the statistical analysis, a set of joining parameters (RS: 2900 rpm, PD: 0.8 mm, JT: 4 s, JP: 0.3 MPa) was

achieved that optimizes the ULSF of the joints. The obtained ULSF with the optimized joining parameters was 2280 ± 88 N.

Regression models for both the PDZ area and ULSF were obtained according to ANOVA. The models could predict the responses with an accuracy of approximately 70% considering a confidence interval of 95%, which is statistically acceptable. Four new joining conditions were designed to validate the regression models. The model for the PDZ area could predict the results for these joints within ±10% error, whereas the generated model for the ULSF predicted three results out of four conditions in the range of ±10% error.

The level of accuracy of the regression models might be increased if the quadratic effect and non-linearity are also taking into account. Therefore, it would be interesting to employ a new DoE, such as response surface methodology (RSM) or central composite design (CCD), which considers the above-mentioned effects of the parameters on the selected responses.

In addition, there is abundant room for investigating the rheological behavior of the molten PPS during the process and the influence of process parameters on the flow of this layer.

Friction spot joints failed in a brittle manner, showing displacement at peak load varying from 0.5 ± 0.0 to 0.8 ± 0.1 mm, as well as failure energy ranging between 0.55 ± 0.04 and 0.97 ± 0.12 J.

It was illustrated that voids and fiber-matrix debonding occur during the joining process as a result of entrapped air in the flowing molten polymer, as well as differences in the shrinkage properties of PPS and carbon fibers. Higher heat input conditions led to a larger area fraction of voids and defects; however, no correlation between the amount of defects and lap shear strength of the joints could be established.

References

[1] Zhang J, Chaisombat K, He S, Wang CH. Hybrid composite laminates reinforced with glass/carbon woven fabrics for lightweight load bearing structures. Mats & Des. 2012;36:75-80.
[2] Mallick PK. Joining for lightweight vehicles. In: Mallick PK, editor. Materials, design and manufacturing for lightweight vehicles. Cambridge: Woodhead Publishing Ltd.; 2010. p. 275-308.
[3] Dursun T, Soutis C. Recent developments in advanced aircraft aluminium alloys. Mats & Des. 2014;56:862-71.

Formatiert: Schriftart: (Standard) +Textkörper CS (Arial)

[4] Li Y, Lu J. Lightweight structure design for wind energy by integrating nanostructured materials. Mats & Des. 2014;57:689-96.

[5] Sedlacek G, Trumpf H. Innovative developments for bridges using FRP composites. Cambridge: Woodhead Publishing Ltd.; 2007.

[6] Marsh G. Composites and Metals – A Marriage of Convenience? Reinforced Plastics. 2014;58:38-42.

[7] Peters ST. Handbook of composites. 2nd ed. London: Chapman & Hall; 1998.

[8] Kinloch AJ, Kodokian GKA. The adhesive bonding of thermoplastic composites. London, England: Imperial College of Science, Technology and Medicine; 1989.

[9] Amancio-Filho ST, dos Santos JF. Method for joining metal and plastic workpieces. European Patent No. EP2329905B1; 2012.

[10] Amancio-Filho ST, Bueno C, dos Santos JF, Huber N, Hage Jr. E. On the feasibility of friction spot joining in magnesium/fiber-reinforced polymer composite hybrid structures. Mater Sci Eng A. 2011;528:3841-8.

[11] Goushegir SM, dos Santos JF, Amancio-Filho ST. Friction Spot Joining of aluminum AA2024/carbon-fiber reinforced poly(phenylene sulfide) composite single lap joints: Microstructure and mechanical performance. Materials and Design. 2014;54:196-206.

[12] Esteves JV, Goushegir SM, dos Santos JF, Canto LB, Hage Jr E, Amancio-Filho ST. Friction spot joining of aluminum AA6181-T4 and carbon fiber-reinforced poly(phenylene sulfide): Effects of process parameters on the microstructure and mechanical strength. Materials and Design. 2014;66 (Part B):437-45.

[13] Anawa EM, Olabi AG. Control of welding residual stress for dissimilar laser welded materials. J Mats Proc Tech. 2008;204:22-33.

[14] Dashatan SH, Azdast T, Ahmadi SR, Bagheri A. Friction stir spot welding of dissimilar polymethyl methacrylate and acrylonitrile butadiene styrene sheets. Materials and Design. 2013;45:135-41.

[15] Altmeyer J, dos Santos JF, Amancio-Filho ST. Effect of the friction riveting process parameters on the joint formation and performance of Ti alloy/short-fibre reinforced polyether ether ketone joints. Materials and Design. 2014;60:164-76.

[16] Huda Z, Taib NS, Zaharinie T. Characterization of 2024-T3: An aerospace aluminum alloy. Mats Chem Phys. 2009;113:515-7.

[17] Davis JR. ASM International: Handbook of Aluminium & Aluminium Alloys. 3rd ed. Ohio1996.

[18] Franchim AS, Fernandez FF, Travessa DN. Microstructural aspects and mechanical properties of friction stir welded AA2024-T3 aluminium alloy sheet. Materials and Design. 2001;32:4684-8.

[19] Amancio-Filho ST, Camillo APC, Bergmann L, dos Santos JF, Kury SE, Machado NGA. Preliminary Investigation of the Microstructure and Mechanical Behaviour of 2024 Aluminium Alloy Friction Spot Welds. Materials Transactions. 2010;52:985-91.

[20] Maruszczak W. Advanced composite polymer for the automotive market; long fiber reinforced linear polyphenylene sulfide (PPS). SPE ACCE conference. Michigan, USA2007.

[21] N.N. Thermoplastic composites for aerospace. The IAPD magazine2010.

[22] N.N. CETEX® PPS, Technical datasheets, Tencate Advanced Composites. Netherlands2009.

[23] Montgomery DC, Runger GC, Hubele NF. Engineering statistics. 5th ed. USA: John Wiley & Sons Inc.; 2011.

[24] Czitrom V, Spagon PD. Statistical Case Studies for Industrial Process Improvement. Philadelphia: Society for Industrial and Applied Mathematics; 1997.

[25] Li XG, Huang MR, Bai H, Yang YL. High-Resolution Thermogravimetry of Polyphenylene Sulfide Film under Four Atmospheres. J App Poly Sci. 2002;83:2053-9.

[26] Ma CCM, Hsia HC, Liu WL, Hu JT. Thermal and Rheological Properties of Poly(Phenylene Sulfide) and Poly(Ether Etherketone) Resins and Composites. Poly Comp. 1987;8:256-64.

[27] Su P, Gerlich A, North T, G B. Energy generation and stir zone dimensions in friction stir spot welds. SAE Technical Paper. 2006:2006-01-0971.

[28] Stokes VK. Analysis of the friction (spin)-welding process for thermoplastics. J Mats Sci. 1988;23:2772-85.

[29] Carslaw HS, Jaeger JC. Conduction of Heat in Solids: Clarendon Press; 1986.

[30] Hou C, Zhao B, Yang J, Yu Z, Wu Q. A Study on Rheologic Behavior of Polyphenylene Sulfide. J Appl Poly Sci. 1995;56:581-90.

[31] Patham B, Foss PH. Thermoplastic Vibration Welding: Review of Process Phenomenology and Processing–Structure–Property Interrelationships. J Poly Eng Sci. 2011;51:1-22.

[32] Gerlich A, Su P, North T. Peak temperatures and microstructures in aluminum and magnesium alloy friction stir spot welds. Sci Tech Weld Joining. 2005;10:647-52.

[33] Gerlich A, Yamamoto M, North T. Local melting and tool slippage during friction stir spot welding of Al-alloys. J Mats Sci. 2008;43:2-11.

[34] Vieille B, Aucher J, Taleb L. Carbon Fiber Fabric Reinforced PPS Laminates: Influence of Temperature on Mechanical Properties and Behavior. Advances in Poly Tech. 2011;30:80-95.

[35] Mandell JF, Huang DD, McGarry FJ. Fatigue of glass and carbon fiber reinforced engineering thermoplastics. Poly Comp. 1981;2:137-44.

[36] Yusof F, Yukio M, Yoshiharu M, Abdul Shukor MH. Effect of anodizing on pulsed Nd:YAG laser joining of polyethylene terephthalate (PET) and aluminium alloy (A5052). Mats & Des. 2012;37:410-5.

[37] Ageorges C, Ye L, Hou M. Experimental investigation of the resistance welding of thermoplastic-matrix composites. Part II: optimum processing window and mechanical performance. Compos Sci Tech. 2000;60:1191-202.

[38] Junior WS, Handge UA, dos Santos JF, Abetz V, Amancio-Filho ST. Feasibility study of friction spot welding of dissimilar single-lap joint between poly(methyl methacrylate) and poly(methyl methacrylate)-SiO2 nanocomposite. Mats & Des. 2014;64:246-50.

[39] Ageorges C, Ye L. Fusion Bonding of Polymer Composites; From Basic Mechanisms to Process Optimization. London, Great Britain: Springer; 2002.

[40] Jung KW, Kawahito Y, Takahashi M, Katayama S. Laser direct joining of carbon fiber reinforced plastic to zinc-coated steel. Mater Des. 2013;47:179-88.

[41] Amancio-Filho ST, Roeder J, Nunes SP, dos Santos JF, Beckmann F. Thermal degradation of polyetherimide joined by friction riveting (FricRiveting). Part I: influence of rotation speed. poly Degradation Stability. 2008;93:1529-38.

[42] Ye L, Chen ZR, Lu M, Hou M. De-consolidation and re-consolidation in CF/PPS thermoplastic matrix composites. Composites: Part A. 2005;36:915-22.

[43] Amanat N, Chaminade C, Grace J, McKenzie DR, James NL. Transmission laser welding of amorphous and semi-crystalline poly-ether–ether–ketone for applications in the medical device industry. Mats & Des. 2010;31:4823-30.
[44] Karachalios EF, Adams RD, da Silva LFM. Strength of single lap joints with artificial defects. Int J Adhes Adhes. 2013;45:69-76.